Chapter 8
Phase transitions in physiologically-based multiscale mean-field brain models

P.A. Robinson, C.J. Rennie, A.J.K. Phillips, J.W. Kim, and J.A. Roberts

8.1 Introduction

Brain dynamics involves interactions across many scales—spatially from microscopic to whole-brain, and temporally from the sub-millisecond range to seconds, or even years. Except under artificial conditions that isolate a single scale, these multiscale aspects of the underlying physiology and anatomy must be included to model the behavior adequately at any scale. In particular, microscale behavior must be included to understand large-scale phase transitions, because the theory of critical phenomena implies that their properties are strongly constrained by the symmetries and conservation properties of the system's microscopic constituents [2].

In condensed matter physics, where they are most familiar, phase transitions arise at the macroscale in systems of atoms, molecules, nuclear spins, or other microscopic constituents. Phase transitions are intrinsically collective properties that are typically analyzed in the thermodynamic limit of infinitely many constituents. They become apparent through discontinuous changes in large-scale order parameters or their derivatives. Examples include the sudden change in density at vaporization or

---

Peter A. Robinson
School of Physics, University of Sydney, NSW 2006, Australia; Brain Dynamics Centre, Westmead Millennium Institute and Westmead Hospital, Westmead, NSW 2145, Australia; Faculty of Medicine, University of Sydney, NSW 2006, Australia.
e-mail: robinson@physics.usyd.edu.au

Christopher J. Rennie
School of Physics, University of Sydney, NSW 2006, Australia; Department of Medical Physics, Westmead Hospital, Westmead, NSW 2145, Australia; Brain Dynamics Centre, Westmead Millennium Institute and Westmead Hospital, Westmead, NSW 2145, Australia.
e-mail: chris_rennie@wmi.usyd.edu.au

Andrew J. K. Phillips · Jong W. Kim · James A. Roberts
School of Physics, University of Sydney, NSW 2006, Australia; Brain Dynamics Centre, Westmead Millennium Institute and Westmead Hospital, Westmead, NSW 2145, Australia.
e-mail: ajp@physics.usyd.edu.au jwkim@physics.usyd.edu.au jamesr@physics.usyd.edu.au

D.A. Steyn-Ross, M. Steyn-Ross (eds.), *Modeling Phase Transitions in the Brain,*
Springer Series in Computational Neuroscience 4, DOI 10.1007/978-1-4419-0796-7_8,

freezing, with an associated nonzero specific heat, or the divergent magnetic susceptibility (derivative of magnetization) at the transition of iron from its nonmagnetic state to a ferromagnetic one with falling temperature, where there is no associated specific heat. Such transitions are termed first-order and second-order, respectively, and occur at *critical points* at which thermodynamic variables such as temperature, pressure, etc., take on highly specific values [2].

Other systems with phase transitions have been identified. Notable are self-organized critical (SOC) systems which self-organize to the critical point, rather than requiring external tuning parameters to be set independently as in thermodynamic transitions. One example is an idealized sandpile growing by the continuous addition of grain, whose slope (the tuning parameter) adjusts itself automatically to very near the critical value at which avalanches commence. The critical slope is then maintained by balance between addition of grains and their loss via avalanches. Criticality in plasma systems has also been shown to be closely associated with microinstabilities of the system that lead to macroscopic changes in the system state [10, 11]. Phase transitions are accompanied by divergent correlation lengths of fluctuations, $1/f$ power-law spectra, and power-law probability distributions of fluctuation amplitudes, the latter two effects implying that critical states inherently involve a wide range of scales in their dynamics.

Mean-field theories provide a natural basis for modeling and analyzing phase transitions in neural systems. Moreover, links to measurements become easy to include—an essential point because most measurement processes aggregate over many neurons and all modify signals in some way. Mean-field theories that incorporate the measurement function are a natural bridge between theoretical and experimental results.

In the class of models described here, averages are taken over microscopic neural structure to obtain mean-field descriptions on scales from tenths of a millimeter up to the whole brain, incorporating representations of the anatomy and physiology of separate excitatory and inhibitory neural populations, nonlinear neural responses, multiscale interconnections, synaptic, dendritic, cell-body, and axonal dynamics, and corticothalamic feedback [4, 7, 12, 14, 16, 17, 24–27, 30–38, 42, 48, 50]. These models readily include measurement effects such as the volume conduction that acts to spatially smooth EEG signals, and the hemodynamic response that temporally filters the BOLD signal that underlies functional MRI.

Essential features of any realistic neurodynamic model are that it: (i) be based on physiology and anatomy, including the salient features at many spatial and temporal scales; (ii) be quantitative with predictions that can be calculated analytically or numerically, including measurement effects; (iii) have parameters that directly relate to physiology and anatomy, and that can be measured, or at least constrained in value, via independent experiments (this does not exclude the theory itself enabling improved estimates of parameters); (iv) be applicable to multiple phenomena and data types, rather than being a theory of a single phenomenon or experimental modality; and (v) be invertible, if possible, allowing parameters to be deduced by fitting model predictions to data (the parameters obtained must be consistent with independent measurements). These criteria rule out (among others) highly idealized models of abstract neurons, as are sometimes used in computer science, theories of single phenomena, or models with parameters highly tailored to single phenomena, models with completely free parameters, and models that take no account of measurement effects.

We have developed a physiologically based mean-field model of brain dynamics that satisfies the above criteria. When applied to the corticothalamic system, it reproduces and unifies many features of EEGs, including background spectra and the spectral peaks seen in waking and sleeping states [32, 34, 37], evoked response potentials [25], measures of coherence and spatiotemporal structure [19, 20, 26, 27], and generalized epilepsies and low-dimensional seizure dynamics [4, 31]. Our approach averages over microstructure to yield mean-field equations in a way that complements cellular-level and neural-network analyses.

In Sect. 8.2 we outline our model, including its physiological and anatomical foundations, basic predictions, and its connection to measurements. In Sects 8.3 and 8.4 we then discuss a range of predictions that relate to neural phase transitions in several regimes, and compare them with experimental data on normal arousal states, epilepsies, and sleep dynamics. Section 8.5 summarizes and discusses the material. We also take the opportunity (in Sects 8.2.1 and 8.3.1) to address a number of fallacies surrounding mean-field theory and its applications, and to highlight open questions (in Sect. 8.5).

8.2 Mean-field theory

In this section we briefly review our model and its connections with measurable quantities. More detailed discussion and further generalizations can be found elsewhere [24, 25, 28, 29, 37].

8.2.1 Mean-field modeling

The brain contains multiple populations of neurons, which we distinguish by a subscript a that designates both the structure in which a given population lies (e.g., a particular nucleus) and the type of neuron (e.g., interneuron, pyramidal cell). We average their properties over scales of $\sim$0.1 mm and seek equations for the resulting mean-field quantities.

The perturbation $V_a(\mathbf{r},t)$ to the mean soma potential is approximated as the sum of contributions $V_{ab}(\mathbf{r},t)$ arriving as a result of activity at each type of (mainly) dendritic synapse b, where b denotes both the population and neurotransmitter type, $\mathbf{r}$ denotes the spatial location, and t the time. This gives

$$V_a(\mathbf{r},t) = \sum_b V_{ab}(\mathbf{r},t). \tag{8.1}$$

The potential V_{ab} is generated when synaptic inputs from afferent neurons are temporally low-pass filtered and smeared out in time as a result of receptor dynamics and passage through the dendritic tree (i.e., by dynamics of ion channels, membranes, etc.). It approximately obeys a differential equation [28, 32, 34, 37]

$$D_{ab}V_{ab}(\mathbf{r},t) = N_{ab}s_{ab}\phi_b(\mathbf{r},t-\tau_{ab}), \tag{8.2}$$

$$D_{ab} = \frac{1}{\alpha_{ab}\beta_{ab}}\frac{\mathrm{d}^2}{\mathrm{d}t^2} + \left(\frac{1}{\alpha_{ab}} + \frac{1}{\beta_{ab}}\right)\frac{\mathrm{d}}{\mathrm{d}t} + 1, \tag{8.3}$$

where $1/\beta_{ab}$ and $1/\alpha_{ab}$ are the rise and decay times of the cell-body potential produced by impulse at a dendritic synapse. The right of Eq. (8.2) describes the influence of the firing rates ϕ_b from neuronal populations b, in general delayed by a time τ_{ab} due to discrete anatomical separations between different structures. The quantity N_{ab} is the mean number of synapses from neurons of type b to type a, and s_{ab} is the time-integrated strength of the response in neurons of type a to a unit signal from neurons of type b, implicitly weighted by the neurotransmitter release probability. Note that we ignore the dynamics of s_{ab}, which can be driven by neuromodulators, firing rate, and other effects; however, such dynamics can be incorporated straightforwardly [5]. An alternative representation of the dynamics in Eq. (8.2) is as a convolution in which

$$V_{ab}(\mathbf{r},t) = \int_{-\infty}^{t} L_{ab}(t-t')N_{ab}s_{ab}\,\phi_b(\mathbf{r},t-t'-\tau_{ab})\,\mathrm{d}t', \tag{8.4}$$

$$L_{ab}(u) = \frac{\alpha_{ab}\beta_{ab}}{\beta_{ab}-\alpha_{ab}}(\mathrm{e}^{-\alpha_{ab}u} - \mathrm{e}^{-\beta_{ab}u}). \tag{8.5}$$

Equation (8.4) is a good approximation to the soma response to a spike input at the dendrites.

In cells with voltage-gated ion channels, action potentials are produced at the axonal hillock when the soma potential exceeds a threshold. In effect, V_a acts as a control variable for the fast spike dynamics, taking the place of the applied current (apart from a capacitive proportionality) characteristic of single-neuron experiments. Spikes in most cortical cells arise via a saddle–node bifurcation in a set of Hodgkin–Huxley-like equations for ionic currents [49]. As such, spikes are produced only for V_a above an individual threshold $\tilde{\theta}_a$, at a mean rate

$$Q_a \propto (V_a - \tilde{\theta}_a)^{1/2}, \tag{8.6}$$

for low Q_a [47], leveling off due to saturation effects at higher V_a [49]. Individual cells differ slightly from the mean in the number and strength of ion channels and, hence, in $\tilde{\theta}_a$. Moreover, fluctuations in V_a affect the difference in (8.6). Hence, the dependence (8.6) must be both modified to include saturation and convolved with an approximately normal distribution of individual deviations to obtain the population-average response function

$$Q_a(\mathbf{r},t) = S[V_a(\mathbf{r},t)], \tag{8.7}$$

where S is a sigmoidal function that increases from 0 to $Q_{\max}$ as V_a increases from $-\infty$ to $+\infty$ [7, 28, 37]. We use the form

$$S[V_a(\mathbf{r},t)] = \frac{Q_{\max}}{1+\exp\{-[V_a(\mathbf{r},t)-\theta_a]/\sigma'\}}, \tag{8.8}$$

where we assume a common mean neural firing threshold θ relative to resting, with $\sigma'\pi/\sqrt{3}$ being its standard deviation (these quantities and $Q_{\max}$ are assumed to be the same for all populations for simplicity). When in the linear regime, we make the approximation

$$Q_a(\mathbf{r},t) = \rho_a V_a(\mathbf{r},t), \tag{8.9}$$

where ρ_a is the derivative of the sigmoid at an assumed steady state of the system in the absence of perturbations (we discuss the existence and stability of such states in later sections).

Each neuronal population a within the corticothalamic system produces a field ϕ_a of pulses, that travels to other neuronal populations at a velocity v_a through axons with a characteristic range r_a. These pulses spread out and dissipate if not regenerated. To a good approximation, this type of propagation obeys a damped wave equation [12, 17, 37]:

$$\mathscr{D}_a\phi_a(\mathbf{r},t) = S[V_a(\mathbf{r},t)], \tag{8.10}$$

$$\mathscr{D}_a = \left(\frac{1}{\gamma_a^2}\frac{\partial^2}{\partial t^2}+\frac{2}{\gamma_a}\frac{\partial}{\partial t}+1-r_a^2\nabla^2\right)\phi_a(\mathbf{r},t), \tag{8.11}$$

where the damping coefficient is $\gamma_a = v_a/r_a$. Equations (8.10) and (8.11) yield propagation ranges in good agreement with anatomical results [3], and with other phenomena. It is sometimes erroneously claimed that this propagation is only an approximation to propagation with delta-function delays of the form $\delta(t-|\mathbf{r}|/v_a)$, and Eq. (8.11) has even been "derived" from the latter under certain assumptions; however, in reality, both are approximations to the true physical situation in the brain.

Equations (8.1)–(8.3), (8.7), (8.8), (8.10), and (8.11) form a closed nonlinear set, which can be solved numerically, or examined analytically in various limits (see Sect. 8.3).

Once a set of specific neural populations has been chosen, and physiologically realistic values have been assigned to their parameters, these equations can be used to make predictions of neural activity. It should be noted that these equations govern spatiotemporal dynamics of firing rates, not of the individual spike dynamics. The two are tightly correlated, but the nonlinearities of our equations are weaker than those that produce the spikes themselves, at least in the sense that they only produce effects on much longer timescales than those of spikes. We stress that the oscillations predicted from our equations are collective oscillations of the rate of spiking, whose frequencies do not directly relate to the frequency of spiking itself—a common misunderstanding of mean-field models by those more familiar with spiking neurons.

8.2.2 Measurements

Once neural activity has been predicted from stimuli, one must relate it to measurements to interpret experimental results. The limited spatiotemporal resolution of such measurements often provides an additional justification for the use of mean-field modeling, since finer-scale structure is not resolvable.

In the case of EEG measurements, the effects of volume conduction on the propagation of neural potential changes to the scalp have been incorporated into our model, via attenuation and spatial filtering parameters [20, 32, 34, 38]. These are included in the bulk of the results reviewed here; space limitations preclude a detailed discussion, but their effects on spectral shape, for example, are slight at frequencies below about 20 Hz, since these correspond to the longest wavelengths. We have also shown how to include the effects of reference electrode and multielectrode derivations [8, 27]. It should also be noted that scalp potentials are primarily generated by excitatory (mainly pyramidal) neurons owing to their greater size and degree of alignment compared to other types [17–19, 25]. For any given geometry, in the linear regime at least, the scalp potential is proportional to the cortical potential, which is itself proportional to the mean cellular membrane currents, which are in turn proportional to ϕ_e. Hence, apart from a (dimensional) constant of proportionality, and the spatial low-pass filtering effects of volume conduction, scalp EEG signals correspond to ϕ_e to a good approximation in the linear domain [36].

8.3 Corticothalamic mean-field modeling and phase transitions

Much work has been done on applications of mean field theory to cortical and corticothalamic systems. Here we consider the latter system since, as discussed below, inclusion of the thalamus is essential if phenomena at typical EEG frequencies are to be successfully modeled.

8.3.1 Corticothalamic connectivities

Figure 8.1 shows the large-scale structures and connectivities incorporated in the model, including the thalamic reticular nucleus r, which inhibits relay (or *specific*) nuclei s, and is lumped here with the perigeniculate nucleus, which has an analogous role [40, 43]. Relay nuclei convey external stimuli ϕ_n to the cortex, as well as passing on corticothalamic feedback. In this section we consider long-range excitatory cortical neurons ($a = e$), short-range mainly inhibitory cortical neurons ($a = i$), neurons in the reticular nucleus of the thalamus ($a = r$), neurons of thalamic relay nuclei ($a = s$), and external inputs ($a = n$) from non-corticothalamic neurons. These populations are discussed further below. Application of these methods to brainstem and hypothalamic structures is discussed in Sect. 8.4.

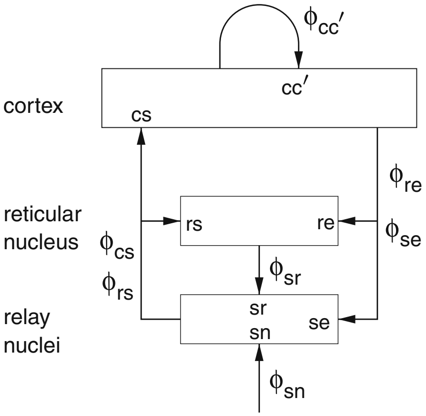

Fig. 8.1 Schematic of corticothalamic interactions, showing the locations at which the ν_{ab} of Eq. (8.12) and linear gains G_{ab} act, where $c, c' = e, i$ denote cortical quantities.

A point that is sometimes overlooked or mistaken in the literature is that mean-field models do not need to divide the cortex into discrete pieces. In particular, there is no need to divide the cortex into hypercolumns, and this is actually likely to be a poor approximation. Indeed, this procedure as it is often implemented is highly misleading, since it imposes sharp hypercolumn boundaries where no such boundaries exist in nature [9]. This is because an anatomical hypercolumn qualitatively corresponds to the region around any given cortical neuron to which that neuron is most strongly connected. A neuron near the boundary of this hypercolumn (which is not sharp in any case) will be strongly connected to neurons on both sides of the boundary (i.e., each neuron lies at the center of its own hypercolumn). So hypercolumn boundaries are not like the walls of a honeycomb, with a fixed physical location, and theoretical approaches that discretize by laying down fixed boundaries must be viewed with some suspicion.

A related misunderstanding in the literature is the idea that short-range and long-range interactions must be treated by different means. This is often encapsulated in a division into short-range connections within hypercolumns and long-range corticocortical connections between hypercolumns, often treated by different mathematical methods. In fact, all connections can be handled using the same formalism, with different ranges simply incorporated via separate neural populations with different axonal range parameters (which does not preclude approximations being made when these ranges are very small) [28].

8.3.2 Corticothalamic parameters

If intracortical connectivities are proportional to the numbers of neurons involved—the *random connectivity approximation*—and $s_{ib} = s_{eb}$, $L_{ib} = L_{eb}$ for each b, then $V_i = V_e$ and $Q_i = Q_e$ [37, 50], which lets us concentrate on excitatory quantities, with inhibitory ones derivable from them. The short range of i neurons and the small size of the thalamic nuclei enables us to assume $r_a \approx 0$ and, hence, $\gamma_a \approx \infty$ for $a = i, r, s$ for many purposes. The only nonzero discrete delays are $\tau_{es} = \tau_{se} = \tau_{re} = t_0/2$, where t_0 is the time for signals to pass from cortex to thalamus and back again. We also assume that all the synaptodendritic time constants are equal, for simplicity, and set $\alpha_{ab} = \alpha$ and $\beta_{ab} = \beta$ for all a and b in what follows; this allows us to drop the subscripts ab in Eqs (8.2), (8.3), and (8.5) and write D_α in place of D_{ab}.

Including only the connections shown in Fig. 8.1 and making the approximations mentioned above, we find that our nonlinear model has 16 parameters (and not all of these appear separately in the linear limit). By defining

$$\nu_{ab} = N_{ab} s_{ab}, \tag{8.12}$$

these are $Q_{\max}$, θ, σ', α, β, γ_e, r_e, t_0, ν_{ee}, ν_{ei}, ν_{es}, ν_{se}, ν_{sr}, ν_{sn}, ν_{re}, and ν_{rs}. These are sufficient in number to allow adequate representation of the most important anatomy and physiology, but few enough to yield useful interpretations and to enable reliable determination of values by fitting theoretical predictions to data. The parameters are approximately known from experiment [28, 29, 32, 34, 38] leading to the indicative values in Table 8.1. We use only values compatible with physiology. Sensitivities of the model to parameter variations have been explored in general [34] and in connection with variations between sleep, wake, and other states [31]. In the present work we concentrate on results for which the model parameters are assumed to be spatially uniform, but where the activity is free to be nonuniform; generalization to include spatial nonuniformities is straightforward [36].

Table 8.1 Indicative parameters for the alert, eyes-open state in normal adults [32]. Parameters used in some figures in this chapter are similar, but not identical.

Quantity	Nominal	Unit
$Q_{\max}$	340	s^{-1}
v_e	10	$\mathrm{m\ s}^{-1}$
r_e	86	mm
θ	13	mV
σ'	3.8	mV
γ_e	116	s^{-1}
α	80	s^{-1}
β	500	s^{-1}
t_0	85	ms
ν_{ee}	1.6	mV s
$-\nu_{ei}$	1.9	mV s
ν_{es}	0.4	mV s
ν_{se}	0.6	mV s
$-\nu_{sr}$	0.45	mV s
ν_{sn}	0.2	mV s
ν_{re}	0.15	mV s
ν_{rs}	0.03	mV s
$\phi_n^{(0)}$	16	s^{-1}

An important implication of the parameters above is that the corticothalamic loop delay t_0 places any oscillations that involve this loop at frequencies of order 10 Hz. This means that inclusion of the thalamus and the dynamics of these loops is essential to understand phenomena at frequencies below $\sim$20 Hz. At very low frequencies ($\ll$ 10 Hz) it is sufficient to include a static corticothalamic feedback strength to the cortex, and at very high frequencies ($\gg$ 10 Hz) the corticothalamic feedback is too slow to affect the dynamics strongly. As we will see in the next section, thalamic effects dominate much of the dynamics at intermediate frequencies.

8.3.3 Specific equations

The above connectivities and parameters imply, using Eqs (8.1)–(8.3),

$$\begin{aligned} D_\alpha V_e(t) &= \nu_{ee}\phi_e(t) + \nu_{ei}\phi_i(t) + \nu_{es}\phi_s(t - t_0/2), && (8.13)\\ D_\alpha V_i(t) &= \nu_{ee}\phi_e(t) + \nu_{ei}\phi_i(t) + \nu_{es}\phi_s(t - t_0/2), && (8.14)\\ D_\alpha V_r(t) &= \nu_{re}\phi_e(t - t_0/2) + \nu_{rs}\phi_s(t), && (8.15)\\ D_\alpha V_s(t) &= \nu_{se}\phi_e(t - t_0/2) + \nu_{sr}\phi_r(t) + \nu_{sn}\phi_n(t), && (8.16) \end{aligned}$$

whence $V_i = V_e$ and $Q_i = Q_e$, as asserted above. The right-hand sides of Eqs (8.13)–(8.16) describe, for each population, the spatial summation of all afferent activity (including via self-connections), and D_α on the left describes temporal dynamics. The short ranges of the axons i, r, and s imply that the corresponding damping rates are large and that $D_\alpha \approx 1$ for these populations, further implying

$$\phi_a = Q_a = S(V_a), \tag{8.17}$$

for $a = i, r, s$. For the remaining e population, Eqs (8.10) and (8.11) yield

$$\left(\frac{1}{\gamma_e^2}\frac{\partial^2}{\partial t^2} + \frac{2}{\gamma_e}\frac{\partial}{\partial t} + 1 - r_e^2\nabla^2\right)\phi_e(\mathbf{r},t) = S[V_e(\mathbf{r},t)], \tag{8.18}$$

with $\gamma_e = v_e/r_e$. Collectively, Eqs (8.13)–(8.18) describe our corticothalamic model.

8.3.4 Steady states

We can find spatially uniform steady states of our system by setting all the spatial and temporal derivatives to zero in Eqs (8.13)–(8.18). The resulting equations can be rearranged to yield a single equation for the steady state value of ϕ_e [32]:

$$0 = S^{-1}\left(\phi_e^{(0)}\right) - (\nu_{ee}+\nu_{ei})\phi_e^{(0)} - \nu_{es}S\left(\nu_{se}\phi_e^{(0)} + \nu_{sn}\phi_n^{(0)}\right.$$
$$\left. + \ \nu_{sr}S\left[\nu_{re}\phi_e^{(0)} + \frac{\nu_{rs}}{\nu_{es}}\left\{S^{-1}\left(\phi_e^{(0)}\right) - (\nu_{ee}+\nu_{ei})\phi_e^{(0)}\right\}\right]\right), \qquad (8.19)$$

where S^{-1} denotes the inverse of the sigmoid function S. The function on the right of Eq. (8.19) is continuous and asymptotes to $-\infty$ as $\phi_e^{(0)} \to 0$ and to $+\infty$ as $\phi_e^{(0)} \to Q_{\max}$. Hence, it has an odd number of zeros, and thus at least one zero [32, 37]. Typically, there is either a single zero or there are three zeros, two stable separated by one unstable in the latter case. For very restricted parameter sets, five zeros (three stable and two unstable at $\omega = 0$, in alternation) are possible, and the addition of neuromodulatory feedbacks on synaptic strengths s_{ab} in Eq. (8.12) can also increase the number of zeros and broaden this parameter range [5]. We mention these generalizations further later, but restrict attention to the main case of three zeros for now.

When there are three zeros, one stable zero occurs at low $\phi_e^{(0)}$, and we identify this as the baseline activity level of normal brain function. The other stable zero is at high $\phi_e^{(0)}$ with all neurons firing near to their physiological maximum. This would thus represent some kind of seizure state, but would require further physiology (e.g., of hemodynamics and hypoxia at these high activity levels) to be treated adequately. The states are shown in Fig. 8.2, where they are linked by the unstable fixed point to form a "fold". It should be noted that other authors have identified the pair of stable states as representing anesthesia/sleep, sleep/wake, or non-REM sleep/REM sleep, often using parameters that lower $\phi_e^{(0)}$ in the upper state to acceptable levels [44–46]. However, they do not seem to have made an overall identification of cases with branches to unify all these possibilities. As we show in Sect. 8.4, brainstem states must be taken into account in this context, so any final identification is probably premature and the above possibilities are not necessarily mutually exclusive.

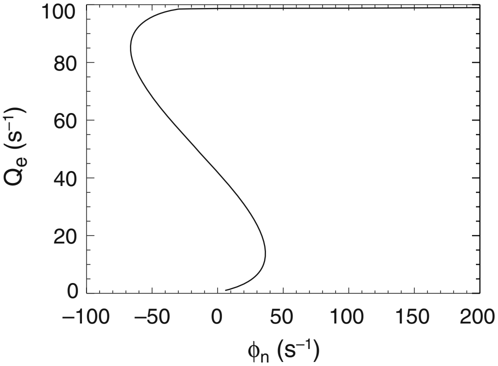

Fig. 8.2 Q_e vs ϕ_n, showing the stable states with low firing rates (< 15 Hz^{-1}) and with firing rates near saturation (> 85 Hz^{-1}). These two branches are linked by an unstable branch to form a "fold". Note that the negative steady state values of ϕ_n in the figure are physical, provided this variable is considered to embody inhibitory neuromodulation, as well as tonic sensory activity.

8.3.5 Transfer functions and linear waves

Small perturbations relative to steady states can be treated using linear analysis. A stimulus $\phi_n(\mathbf{k},\omega)$ of angular frequency ω ($= 2\pi f$, where f is the usual frequency in Hz) and wave vector $\mathbf{k}$ ($= 2\pi/\lambda$ in magnitude, where λ is the wavelength) has the transfer function to $\phi_e(\mathbf{k},\omega)$

$$\frac{\phi_e(\mathbf{k},\omega)}{\phi_n(\mathbf{k},\omega)} = \frac{G_{es}L}{1-G_{ei}L}\frac{G_{sn}Le^{i\omega t_0/2}}{1-G_{srs}L^2}\frac{1}{q^2(\omega)r_e^2+k^2r_e^2}, \tag{8.20}$$

$$q^2(\omega)r_e^2 = (1-i\omega/\gamma_e)^2 - \frac{L}{1-G_{ei}L}\left[G_{ee}+\frac{(G_{ese}+G_{esre}L)L}{1-G_{srs}L^2}e^{i\omega t_0}\right], \tag{8.21}$$

$$G_{ab} = \frac{\phi_a^{(0)}}{\sigma'}\left(1-\frac{\phi_a^{(0)}}{Q_{\max}}\right)\nu_{ab}, \tag{8.22}$$

where $L = (1-i\omega/\alpha)^{-1}(1-i\omega/\beta)^{-1}$ embodies the lowpass filter characteristics of synaptodendritic dynamics and $\phi_a^{(0)}$ is the steady-state value of ϕ_a. The ratio (8.20) is the cortical excitatory response per unit external stimulus, and encapsulates the relative phase via its complex value [25, 28, 34]; it is the key to linear properties of the system. The gain G_{ab} is the differential output produced by neurons a per unit change in input from neurons b, and the static gains for loops in Fig. 8.1 are $G_{ese} = G_{es}G_{se}$ for feedback via relay nuclei only, $G_{esre} = G_{es}G_{sr}G_{re}$ for the loop through reticular and relay nuclei, and $G_{srs} = G_{sr}G_{rs}$ for the intrathalamic loop.

Waves obey the dispersion relation [37]

$$q^2(\omega)+k^2 = 0, \tag{8.23}$$

which corresponds to singularity of the transfer function (8.20). Solutions of this equation satisfy $\omega = kv_e - i\gamma_e$ at high frequencies [37]. At lower frequencies, their dispersion has been investigated in detail previously [19, 24, 37].

8.3.6 Spectra

The EEG frequency spectrum is obtained by squaring the modulus of $\phi_e(\mathbf{k},\omega)$ and integrating over $\mathbf{k}$. It can be written in terms of the transfer function (8.20) as

$$P_e(\omega) = \int\left|\frac{\phi_e(\mathbf{k},\omega)}{\phi_n(\mathbf{k},\omega)}\right|^2|\phi_n(\mathbf{k},\omega)|^2\,\mathrm{d}^2\mathbf{k}. \tag{8.24}$$

If we make the assumption that under conditions of spontaneous EEG the field of external stimuli $\phi_n(\mathbf{k},\omega)$ is so complex that it can be approximated by spatiotemporal white noise, this gives $|\phi_n(\mathbf{k},\omega)|^2 = \text{const}$. In the white noise case

$$P_e(\omega) = \frac{\langle \phi_n^2 \rangle}{4\pi r_e^4} \left| \frac{G_{esn}L^2}{(1 - G_{ei}L)(1 - G_{srs}L^2)} \right|^2 \frac{\operatorname{Arg} q^2}{\operatorname{Im} q^2}, \tag{8.25}$$

where $\langle \phi_n^2 \rangle$ is the mean-square noise level. Figure 8.3 shows shows excellent agreement of Eq. (8.25) with an observed spectrum over several decades. The features reproduced include the alpha and beta peaks at frequencies $f \approx 1/t_0, 2/t_0$, and the asymptotic low- and high-frequency behaviors; key differences between waking and sleep spectra can also be reproduced, including the strong increase in low-frequency activity in sleep, where our model predicts a steepening of the spectrum from $1/f$ to $1/f^3$ [34]. Notably, each of the features can be related to underlying anatomy and physiology. The low-frequency $1/f$ behavior is a signature of marginally stable, near-critical dynamics, which allow complex behavior [31, 34, 37], while the steep high-frequency fall-off results from low-pass filtering by synaptodendritic dynamics. Corticothalamic loop resonances account for the alpha and beta peaks, their relative frequencies, the correlated changes in spectral peaks between sleep and waking, and splitting of the alpha peak, for example [31, 34, 36]. Suggested alternative mechanisms, including pacemakers and purely cortical resonances, can account for some features of the data, but the trend in mode frequency predicted for purely cortical eigenmodes tends to be in the opposite direction to that observed, although this is not unequivocal. Likewise, the pacemaker hypothesis is ad hoc, with a new pacemaker proposed for every spectral peak [17, 30, 36]. Overall, the evidence is now strong that the thalamus must be included to account for most salient EEG features at frequencies below about 20 Hz. The advantage of its inclusion is underlined by the ability of the resulting theory to simultaneously account for the wide range of phenomena mentioned in Sect. 8.1.

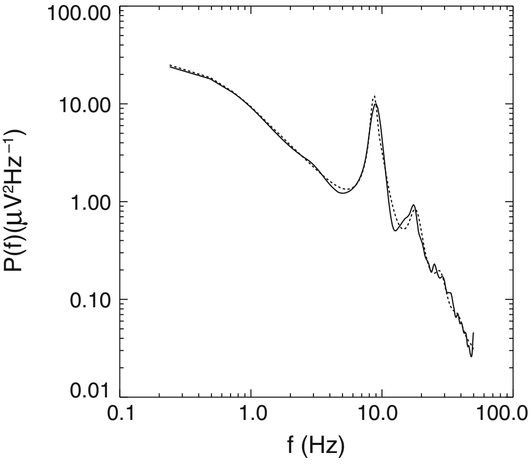

Fig. 8.3 Example spectrum (solid) and model fit (dashed) from a typical adult subject in the eyes-closed state.

One key aspect of phase transitions is the divergent correlation length near the critical point, mentioned above. Correlations and coherence can be computed using our theory. Specifically, the Wiener–Khintchine theorem implies that the correlation function is the Fourier transform of the power spectrum, which yields long-range correlations at sharp spectral peaks, with the correlation length increasing in proportion to the quality factor of the peak [27]. This accords with these waves being weakly damped (and thus close to instability) and so able to propagate large distances at high amplitudes.

The cross spectrum $P_e(\mathbf{r},\mathbf{r}',\omega)$ is the phase average of $\phi_e(\mathbf{r},\omega)\phi_e^*(\mathbf{r}',\omega)$, which can be computed via the spatial Fourier transform of $\phi_e(\mathbf{k},\omega)$. The coherence function is then

$$\gamma^2(\mathbf{r},\mathbf{r}',\omega) = \frac{[P_e(\mathbf{r},\mathbf{r}',\omega)]^2}{P_e(\mathbf{r},\mathbf{r},\omega)P_e(\mathbf{r}',\mathbf{r}',\omega)}. \tag{8.26}$$

This result has been shown to give good agreement with observations of γ^2 as a function of frequency at fixed separation for model parameters close to those used in obtaining the other plots in this work [27, 41]. Particular features are that coherence peaks correspond to spectral peaks, reflecting the fact that weakly damped waves can reach high amplitudes (hence a spectral peak) and propagate far before dissipating (hence high coherence).

8.3.7 Stability zone, instabilities, seizures, and phase transitions

Linear waves obey the dispersion relation (8.23), with instability boundaries occurring where this equation is satisfied for real ω [31, 34, 37]. In most circumstances, waves with $k = 0$ (i.e., spatially uniform) are the most unstable [37], and it is found that only the first few (i.e., lowest frequency) spectral resonances can become unstable. Analysis of stability of perturbations relative to the steady state that represents normal activity for realistic parameter ranges finds just four $k = 0$ instabilities, leading to global nonlinear dynamics [4, 31, 33]: (a) Slow-wave instability ($f \approx 0$) via a saddle–node bifurcation that leads to a low frequency spike-wave limit cycle; (b) theta instability, via a supercritical Hopf bifurcation that saturates in a nonlinear limit cycle near 3 Hz, with a spike-wave form unless its parameters are close to the instability boundary; (c) alpha instability, via a subcritical Hopf bifurcation, giving a limit cycle near 10 Hz; and (d) spindle instability at $\omega \approx (\alpha\beta)^{1/2}$, leading to a limit cycle at 10–15 Hz (the nature of this bifurcation has not yet been investigated). The boundaries defined by these instabilities are interpreted as corresponding to onsets of generalized seizures, as discussed in more detail below [4, 31, 33].

The occurrence of only a few instabilities, at low frequencies, enables the state and physical stability of the brain to be represented in a 3-D space with axes

$$x = G_{ee}/(1 - G_{ei}), \tag{8.27}$$

$$y = (G_{ese} + G_{esre})/[(1 - G_{srs})(1 - G_{ei})], \tag{8.28}$$

$$z = -G_{srs}\alpha\beta/(\alpha + \beta)^2, \tag{8.29}$$

which parameterize cortical, corticothalamic, and thalamic stability, respectively [4, 31]. In terms of these quantities, parameters corresponding to linearly stable brain states lie in a stability zone illustrated in Fig. 8.4. The back is at $x = 0$ and the base at $z = 0$. A pure spindle instability occurs at $z = 1$, which couples to the alpha instability, with spindle dominating at top and left, and alpha at right. At small z, the left surface is defined by a theta instability [4, 31]. The front right surface corresponds to slow-wave instability at $x + y = 1$.

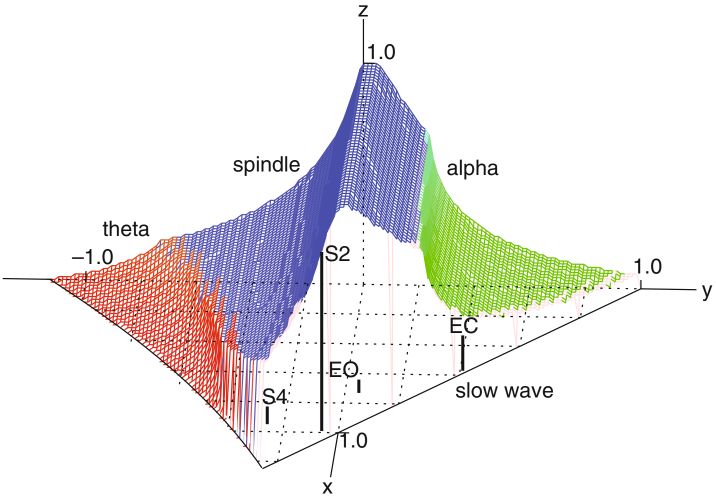

Fig. 8.4 [Color plate] Brain stability zone. The surface is shaded according to instability, as labeled (blue = spindle, green = alpha, red = theta), with the front right-hand face left transparent as it corresponds to a slow-wave instability. Approximate locations are shown of alert eyes-open (EO), relaxed, eyes-closed (EC), sleep stage 2 (S2), and sleep stage 4 (S4) states, with each state located at the top of its bar, whose (x, y) coordinates can be read from the grid.

Non-seizure states lie within the stability zone in Fig. 8.4. Detailed arguments regarding the sign of feedback via the thalamus, proximity between neighboring behavioral states, and the results of explicit fitting to data (which is enabled by using the present model), place the arousal sequence, from alert eyes-open (EO) to deep sleep, including relaxed eyes-closed (EC) and sleep stages 1–4 (S1–S4), as shown in Fig. 8.4 [31]. In future, it is expected that known differences between EEG spectra for subjects with differing disorders will also enable classification of these conditions into different parts of the stability zone.

Two of the most common generalized epilepsies are absence and tonic-clonic seizures. In absence epilepsy, seizures last 5–20 s, cause loss of consciousness, show a spike-wave cycle which starts and stops abruptly across the whole scalp, and the subject reaches a post-seizure state similar to the pre-seizure one. Tonic-clonic seizures display a tonic phase of roughly 10 Hz oscillations lasting about 10 s, followed by a clonic phase of similar duration dominated by polyspike-wave complexes, with an unresponsive post-seizure state very different from the pre-seizure one [4, 15, 41]. Figures 8.5(a) and (b) show results from our model under conditions for theta and alpha instability, respectively. In Fig. 8.5(a) the onset of an approximately 3-Hz spike-wave cycle is seen as the system is forced across the instability boundary by ramping one of its parameters, in this case ν_{se}. This closely resembles observed absence time series [4, 6, 31, 33]. If the destabilizing parameter is ramped back, the system returns smoothly to very nearly its initial state, consistent with clinical observations. Figure 8.5(b) shows good agreement with generalized tonic-clonic seizure dynamics near 10 Hz. However, in this case, the limit cycle sets in with nonzero amplitude. Moreover, when the control parameter is ramped back, hysteresis is observed, with the limit cycle terminating to yield a different final state, with a quiescent time series, consistent with clinical observations [4, 15].

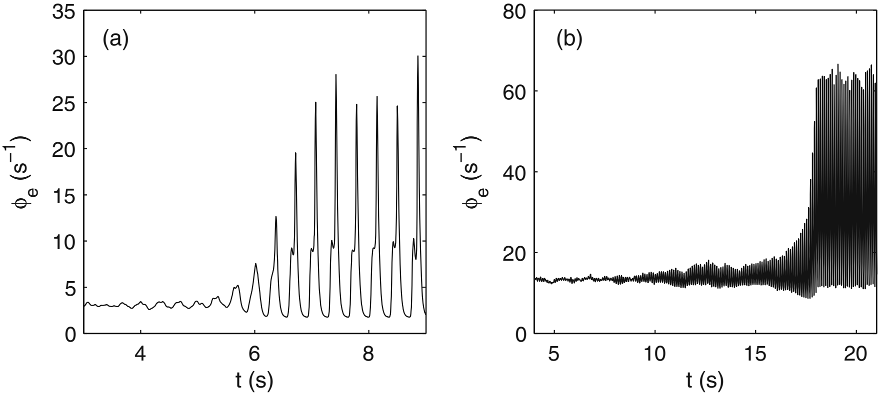

Fig. 8.5 Sample time series from the model in regimes corresponding to onset of (a) an absence seizure, and (b) a tonic-clonic seizure.

Each of the above instabilities can be seen as a phase transition. The saddle–node bifurcation is marked by a spectral divergence at $f = 0$, a $1/f$ spectrum at low f, and long-range correlations and coherence. There is also a divergence of the variance of ϕ_e, which can be approximated by integrating $P_e(\omega)$ over ω to yield the scaling

$$\left\langle \left[\phi_e - \phi_e^{(0)}\right]^2 \right\rangle \propto \left[V_{SN} - V_n^{(0)}\right]^{-1/2}, \tag{8.30}$$

where the angle brackets denote an average, the mean external input $V_n^{(0)}$ is the control parameter for the transition, and V_{SN} is its value at the bifurcation. This result accords with numerical results for such a transition [44] and related analysis of single neurons [45] (see also Sect. 8.4).

One recently explored feature of the nonzero-f limit cycles is that these can be initiated in localized regions of the system, and then spread to other areas, qualitatively consistent with clinical observations of secondary seizure generalization from a focus [13]. In this case, the boundary between seizing and normal zones propagates in a manner akin to a domain boundary between solid and liquid in a spatially nonuniform melting/freezing transition. An example is shown in Fig. 8.6 [13].

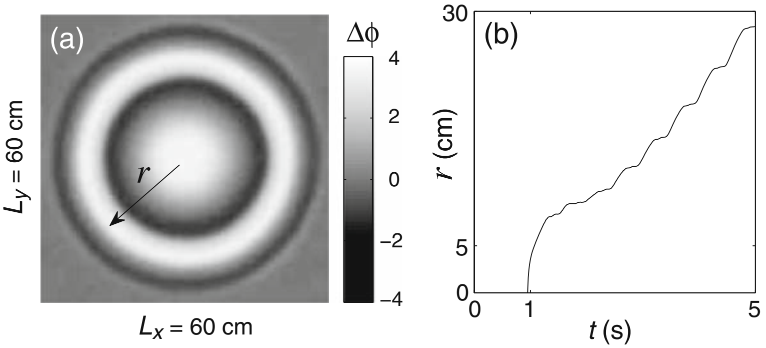

Fig. 8.6 Spreading of seizure activity from an initial focus. The figure shows (a) a snapshot of $\phi(\mathbf{r},t)$, and (b) the linear spread of the wave following a stimulus at $t = 1$ s.

8.4 Mean-field modeling of the brainstem and hypothalamus, and sleep transitions

Wake-sleep transitions are primarily governed by the nuclei of the ascending arousal system of the brainstem and hypothalamus, that project diffusely to the corticothalamic system. As we will see shortly, these nuclei are also capable of undergoing instabilities and phase transitions in their dynamics. Hence, a full description of sleep–wake transitions and their EEG correlates requires an integrated model of both the ascending arousal system and the corticothalamic system (at least), including their mutual interactions. This section briefly describes how the nuclei of the Ascending Arousal System (AAS) are modeled using the same methods as above, and outlines the direction of integration of the two models, currently under way. In this section, observables consist of arousal states (sleep vs. wake), so other measurement effects need not be taken into account.

8.4.1 Ascending Arousal System model

The most important nuclei to model in the AAS are well established from detailed physiological investigations, and are shown in Fig. 8.7. These include the monoaminergic (MA) group and the ventrolateral preoptic nucleus (VLPO), which mutually inhibit one another, resulting in flip-flop dynamics if the interaction is sufficiently strong—only one can be active at a time, and it suppresses the other

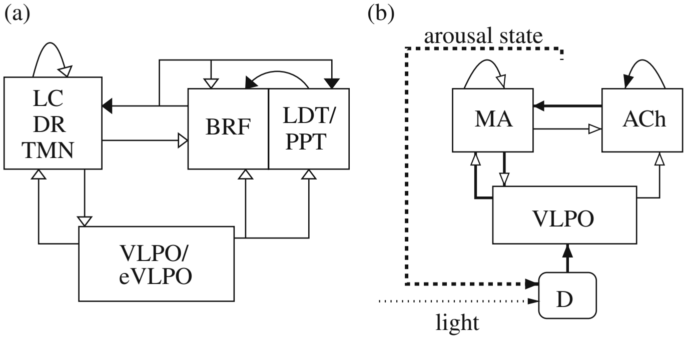

Fig. 8.7 Parts (a) and (b) show schematics of the actual AAS populations, and our sleep model, respectively. Excitatory inputs are represented by solid arrow heads, and inhibitory by open ones. In each case, the top left box is the MA group, and the top right box is the ACh group. In (a), the MA group consists of the LC, DR (dorsal raphe) and TMN (tuberomamillary nucleus); and the ACh group consists of cholinergic LDT/PPT, and glutamergic BRF. The VLPO/eVLPO GABAergically inhibits other AAS nuclei. In (b) the drive D is shown, which consists of circadian (C) and homeostatic (H) components. In our model the thick-lined interactions in (b) are used.

[39]. During wake, the MA group is dominant, while the VLPO is dominant in sleep. Transitions between states are driven by inputs to the VLPO, which include the circadian drive C (mainly from light exposure), and the homeostatic sleep drive H arising from net buildup of metabolic byproducts (mostly adenosine) during wake, and their net clearance during sleep. There is also an input to the MA group from cholinergic and orexinergic nuclei, as shown [21, 39].

Until recently, models of AAS dynamics have been either nonmathematical (e.g., based on sleep diaries or qualitative considerations) or abstract (mathematical, but not derived directly from physiology). The widely known *two-process model* is of the latter form, and includes circadian and homeostatic influences [1]. In this section, which summarizes our recent model of the AAS [22], we use the same methods as in Sects 8.2–8.3 to model the dynamics of the AAS nuclei, viewing them as the assemblies of neurons they are. Several simplifications and approximations are appropriate: the nuclei are small, so $r_a \approx 0$ and $\gamma_a \to \infty$ in Eq. (8.11), implying that Eq. (8.17) applies for these nuclei. Also, since the transitions take place on timescales of many seconds to minutes, first-order in time versions of Eq. (8.3) can be used. We also assume that, since the system spends little time in transitions, the generation rate of H has just two values—one for wake and one for sleep—and that its clearance rate is proportional to H, while the variation of C is approximated as sinusoidal. These approximations yield

$$\tau \frac{dV_v}{dt} + V_v = \nu_{vm} Q_m + D, \tag{8.31}$$

$$\tau \frac{dV_m}{dt} + V_m = \nu_{mv} Q_v + A, \tag{8.32}$$

$$\chi\frac{dH}{dt}+H=\mu Q_m, \tag{8.33}$$

$$Q_a=S(V_a), \tag{8.34}$$

$$C=c_0+\cos(\Omega t), \tag{8.35}$$

$$D=\nu_{vc}C+\nu_{vh}H, \tag{8.36}$$

where the time constants τ of the nuclear responses have been assumed equal [these replace $1/\alpha$ in (8.3), with $\beta\to\infty$ formally], χ is the adenosine clearance time, v denotes VLPO, m denotes monoaminergic nuclei, the ν_{ab}, V_a, and Q_a have the same meanings as in previous sections, μ gives the proportionality between monoaminergic activity and adenosine generation rate, C_A is the amplitude of the C cycle, and $\Omega=2\pi/(1\,\text{day})$.

In the above form the model has 12 physiological parameters: τ, χ, ν_{vm}, ν_{mv}, A, μ, c_0, ν_{vc}, ν_{vh}, $Q_{\max}$, θ, and σ', whose nominal values are given in Table 8.2. These values were determined by a combination of physiological constraints from the literature, and comparison of the dynamics with behavior in a restricted set of sleep experiments on normal sleep and sleep deprivation [22, 23]. The theory then predicts other phenomena in regimes outside those of the calibration experiments.

In the context of the present chapter, the key result is that the steady states of Eqs (8.31)–(8.36) display a “fold” as a function of the total drive D. The upper and lower branches represent wake and sleep, respectively, with an unstable branch in between. Cyclic variations in D cause the system to move around the hysteresis loop shown in Fig. 8.8, with saddle–node bifurcations from wake to sleep and back again. In the presence of noise added to D on the right of Eq. (8.31), Fig. 8.9 shows that these are preceded by divergences in V_m fluctuations that satisfy the same power-law scaling as Eq. (8.30) for subtheshold noise, and lead to what appear to be microsleeps and microwakes in the vicinity of the transition for larger amplitude noise. Narcolepsy, with its lack of stability of wake and sleep is then interpreted as resulting from a reduction or disappearance of the hysteresis loop [22].

Table 8.2 Nominal parameter values for the ascending arousal system model.

Quantity	Nominal	Unit
$-\nu_{vc}$	2.9	mV
ν_{vh}	1.0	mV nM^{-1}
χ	45	h
μ	4.4	nM s
c_0	4.5	–
$Q_{\max}$	100	s^{-1}
θ	10	mV
σ'	3	mV
A	1.3	mV
$-\nu_{vm}$	2.1	mV s
$-\nu_{mv}$	1.8	mV s
τ	10	s

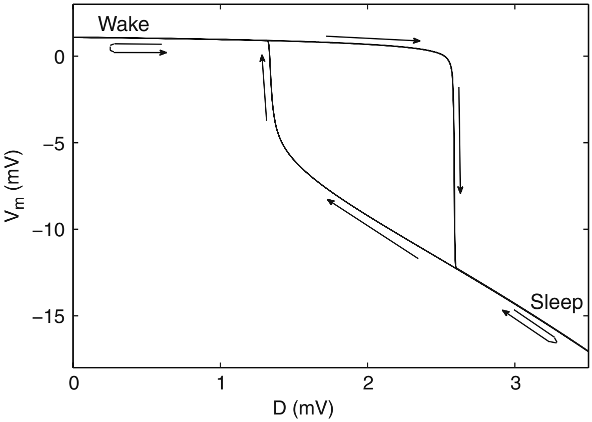

Fig. 8.8 Plot of V_m versus the sleep drive D across a 24 h period. As D oscillates across the day, V_m cycles around a hysteresis loop between wake and sleep states.

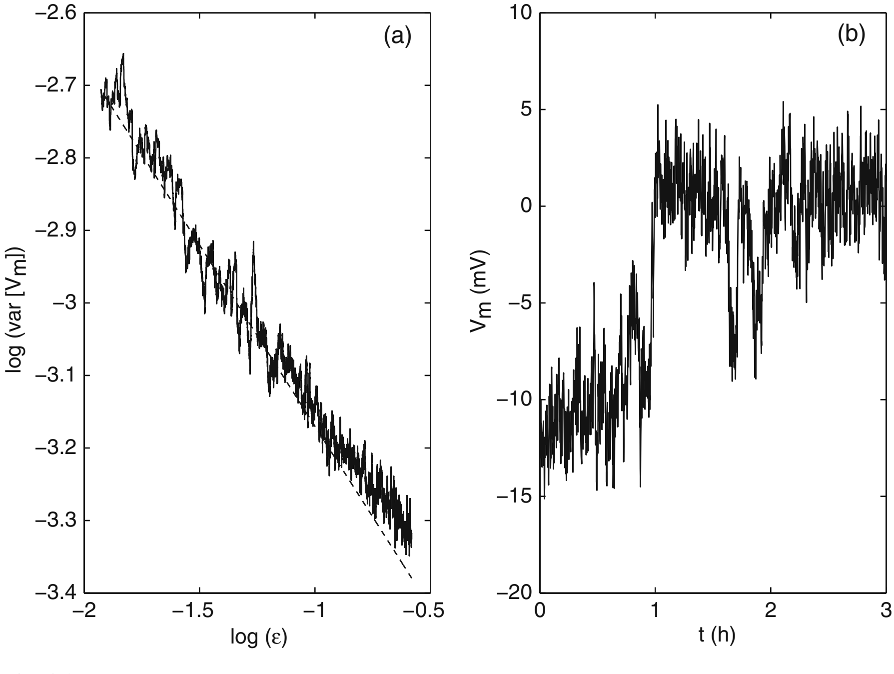

Fig. 8.9 (a) Log-log plot of the variance of V_m in the presence of low amplitude noise (solid), versus $\varepsilon = D - D_0$, where D_0 is the value of D for which the wake state loses stability. D is increased linearly at a rate of 7×10^{-5} h^{-1}, and variance is calculated in moving windows of length 17 h. The asymptotic gradient of -0.5 is shown as a dashed line. (b) Transitions between high V_m (wake) and low V_m (sleep) in the presence of high amplitude noise.

This set of outcomes implies that inclusion of the dynamics of the AAS is essential to understand sleep–wake cycles, although work is still under way to incorporate the ascending projections to the corticothalamic system quantitatively, feedback in the reverse direction, and quantitative models of the circadian pathway, involving the suprachiasmatic nucleus (SCN).

8.5 Summary and discussion

Physiologically based mean-field theories of the brain are able to incorporate essential physiology and anatomy across the many scales necessary to treat phase transitions and other phenomena involving neural activity. They can achieve this for physiologically realistic parameters, and yield numerous predictions that accord with observations using a variety of experimental methods in both the linear and nonlinear regimes (see Sect. 8.1). Moreover, they do this in a way that unifies what have hitherto been disparate subfields and measurement modalities within a single framework, and which permits parameter determination via fits of model predictions to experimental data. In addition to these specific results, major qualitative conclusions that are reached using such models include the necessity of incorporating the thalamus to understand EEG phenomena at frequencies below about 20 Hz, and the need to include the ascending arousal system to understand sleep–wake dynamics.

In the area of phase transitions, mean-field modeling successfully predicts the connections between transitions, instabilities, long-range correlations and coherence, spectral peaks, and divergences of variance in a number of regimes. However, much remains to be done in directions such as the fuller integration of multiple brain subsystems into unified models, exploration of the dynamics of neuromodulators and behavioral feedbacks, and application to other putative phase transitions in areas such as visual rivalry and perception, parkinsonian tremor onset, and possibly bipolar disorder. One could also investigate whether some Hopf bifurcations (e.g., supercritical ones) correspond to second-order phase transitions, as opposed to the first-order ones investigated here, and whether the variance divergences seen near criticality have a role in control or prevention of phase transitions.

Acknowledgments The Australian Research Council supported this work.

References

1. Achermann, P., Borbély, A.A.: Mathematical models of sleep regulation. Front. Biosci. **8**, s683–s693 (2003)
2. Binney, J.J., Dowrick, N.J., Fisher, A.J., Newman, M.E.J.: The Theory of Critical Phenomena. Clarendon Press, Oxford (1992)

3. Braitenberg, V., Shüz, A.: Anatomy of the Cortex: Statistics and geometry. Springer, Berlin (1991)
4. Breakspear, M., Roberts, J.A., Terry, J.R., Rodrigues, S., Mahant, N., Robinson, P.A.: A unifying explaination of primary generalized seizures through nonlinear brain modeling and bifurcation analysis. Cerebral Cortex **16**, 1296–1313 (2006), doi:10.1093/cercor/bhj072
5. Clearwater, J.M., Rennie, C.J., Robinson, P.A.: Mean field model of acetylcholine mediated dynamics in the cerebral cortex. Biol. Cybernetics **97**, 449–460 (2007), doi:10.1007/s00422-007- 0186-9
6. Feucht, M., Möller, U., Witte, H., Schmidt, K., Arnold, M., Benninger, F., Steinberger, K., Friedrich, M.H.: Nonlinear dynamics of 3 Hz spike-and-wave discharges recorded during typical absence seizures in children. Cerebral Cortex **8**(6), 524–533 (1998)
7. Freeman, W.J.: Mass Action in the Nervous System. Academic Press, New York (1975)
8. Henderson, J.A., Phillips, A.J.K., Robinson, P.A.: Multielectrode electroencephalogram power spectra: Theory and application to approximate correction of volume conduction effects. Phys. Rev. E **73**, 051918 (2006), doi:10.1103/PhysRevE.73.051918
9. Horton, J.C., Adams, D.L.: The cortical column: A structure without a function. Philos. Trans. Roy. Soc. Lond. Ser. B **360**, 837–862 (2005), doi:10.1098/rstb.2005.1623
10. Ivanov, A.V., Cairns, I.H., Robinson, P.A.: Wave damping as a critical phenomenon. Phys. Plasmas **10**, 4649–4661 (2004), doi:10.1063/1.1785789
11. Ivanov, A.V., Vladimirov, S.V., Robinson, P.A.: Criticality in a Vlasov-Poisson system: A fermioniclike universality class. Phys. Rev. E **71**, 056406 (2005), doi:10.1103/PhysRevE.71.056406
12. Jirsa, V.K., Haken, H.: Field theory of electromagnetic brain activity. Phys. Rev. Lett. **77**, 960–963 (1996)
13. Kim, J.W., Roberts, J.A., Robinson, P.A.: Dynamics of epileptic seizures: Evolution, spreading, and suppression. J. Theor. Biol. 257(4), 527–532 (2009), doi:10.1016/j.jtbi.2008.12.009
14. Lopes da Silva, F.H., Hoeks, A., Smits, H., Zetterberg, L.H.: Model of brain rhythmic activity. T alpha-rhythm of the thalamus. Kybernetik **15**, 27–37 (1974)
15. Niedermeyer, E.: The normal EEG of the waking adult. In: E. Niedermeyer, F. Lopes da Silva (eds.), Electroencephalography: Basic Principles, Clinical Applications, and Related Fields, pp. 149–173, Williams & Wilkins, Baltimore, fourth edn. (1999)
16. Nunez, P.L.: The brain wave equation: A model for the EEG. Math. Biosci. **21**, 279–297 (1974)
17. Nunez, P.L.: Neocortical Dynamics and Human EEG Rhythms. Oxford University Press, New York (1995)
18. Nunez, P.L., Srinivasan, R.: Electric Fields of the Brain : The Neurophysics of EEG. Oxford University Press, New York, 2nd edn. (2006)
19. O'Connor, S.C., Robinson, P.A.: Wave-number spectrum of electrocorticographic signals. Phys. Rev. E **67**, 051912 (2003), doi:10.1103/PhysRevE.67.051912
20. O'Connor, S.C., Robinson, P.A., Chiang, A.K.I.: Wave-number spectrum of electroencephalographic signals. Phys. Rev. E **66**, 061905 (2002), doi:10.1103/PhysRevE.66.061905
21. Pace-Schott, E.F., Hobson, J.A.: The neurobiology of sleep: Genetics, cellular physiology and subcortical networks. Nature Rev. Neurosci. **3**, 591–605 (2002), doi:10.1038/nrn895
22. Phillips, A.J.K., Robinson, P.A.: A quantitative model of sleep-wake dynamics based on the physiology of the brainstem ascending arousal system. J. Biol. Rhythms **22**(2), 167–179 (2007), doi:10.1177/0748730406297512
23. Phillips, A.J.K., Robinson, P.A.: Sleep deprivation in a quantitative physiologically-based model of the ascending arousal system. J. Theor. Biol. 255(4), 413–423 (2008), doi:10.1016/j.jtbi.2008.08.022
24. Rennie, C.J., Robinson, P.A., Wright, J.J.: Effects of local feedback on dispersion of electrical waves in the cerebral cortex. Phys. Rev. E **59**(3), 3320–3329 (1999)
25. Rennie, C.J., Robinson, P.A., Wright, J.J.: Unified neurophysical model of EEG spectra and evoked potentials. Biol. Cybernetics **86**, 457–471 (2002), doi:10.1007/s00422-002-0310-9

26. Robinson, P.A.: Interpretation of scaling properties of electroencephalographic fluctuations via spectral analysis and underlying physiology. Phys. Rev. E **67**, 032902 (2003), doi:10.1103/PhysRevE.67.032902
27. Robinson, P.A.: Neurophysical theory of coherence and correlations of electroencephalographic and electrocorticographic signals. J. Theor. Biol. **222**, 163–175 (2003), doi:10.1016/j.jtbi.2004.07.003
28. Robinson, P.A.: Propagator theory of brain dynamics. Phys. Rev. E **72**, 011904 (2005), doi:10.1103/PhysRevE.72.011904
29. Robinson, P.A.: Patchy propagators, brain dynamics, and the generation of spatially structured gamma oscillations. Phys. Rev. E **73**, 041904 (2006), doi:10.1103/PhysRevE.73.041904
30. Robinson, P.A., Loxley, P.N., O'Connor, S.C., Rennie, C.J.: Modal analysis of corticothalamic dynamics, electroencephalographic spectra, and evoked potentials. Phys. Rev. E **63**(4), 041909 (2001), doi:10.1103/PhysRevE.63.041909
31. Robinson, P.A., Rennie, C.J., Rowe, D.L.: Dynamics of large-scale brain activity in normal arousal states and epileptic seizures. Phys. Rev. E **65**(4), 041924 (2002), doi:10.1103/PhysRevE.65.041924
32. Robinson, P.A., Rennie, C.J., Rowe, D.L., O'Connor, S.C.: Estimation of multiscale neurophysiologic parameters by electroencephalographic means. Hum. Brain Mapp. **23**, 53–72 (2004), doi:10.1002/hbm.20032
33. Robinson, P.A., Rennie, C.J., Rowe, D.L., O'Connor, S.C., Wright, J.J., Gordon, E., Whitehouse, R.W.: Neurophysical modeling of brain dynamics. Neuropsychopharmacology **28**, s74–s79 (2003), doi:10.1038/sj.npp.1300143
34. Robinson, P.A., Rennie, C.J., Wright, J.J., Bahramali, H., Gordon, E., Rowe, D.L.: Prediction of electroencephalographic spectra from neurophysiology. Phys. Rev. E **63**(2), 021903 (2001), doi:10.1103/PhysRevE.63.021903
35. Robinson, P.A., Rennie, C.J., Wright, J.J., Bourke, P.: Steady states and global dynamics of electrical activity in the cerebral cortex. Phys. Rev. E **58**(3), 3557–3571 (1998)
36. Robinson, P.A., Whitehouse, R.W., Rennie, C.J.: Nonuniform corticothalamic continuum model of electroencephalographic spectra with application to split-alpha peaks. Phys. Rev. E **68**, 021922 (2003), doi:10.1103/PhysRevE.68.021922
37. Robinson, P.A., Rennie, C.J., Wright, J.J.: Propagation and stability of waves of electrical activity in the cerebral cortex. Phys. Rev. E **56**(1), 826–840 (1997)
38. Rowe, D.L., Robinson, P.A., Rennie, C.J.: Estimation of neurophysiological parameters from the waking EEG using a biophysical model of brain dynamics. J. Theor. Biol. **231**, 413–433 (2004), doi:10.1016/j.jtbi.2004.07.004
39. Saper, C.B., Chou, T.C., Scammell, T.E.: The sleep switch: hypothalamic control of sleep and wakefulness. Trends Neurosci. **24**, 726–731 (2001), doi:10.1016/S0166-2236(00)02002-6
40. Sherman, S.M., Guillery, R.W.: Exploring the Thalamus. Academic Press (2001)
41. Srinivasan, R., Nunez, P.L., Silberstein, R.B.: Spatial filtering and neocortical dynamics: Estimates of EEG coherence. IEEE Trans. Biomed. Eng. **45**, 814–826 (1998)
42. Steriade, M., Gloor, P., Llinás, R.R., Lopes da Silva, F.H., Mesulam, M.M.: Basic mechanisms of cerebral rhythmic activities. Electroenceph. Clin. Neurophysiol. **76**, 481–508 (1990)
43. Steriade, M., Jones, E.G., McCormick, D.A. (eds.): Thalamus (2 vols). Elsevier, Amsterdam (1997)
44. Steyn-Ross, D.A., Steyn-Ross, M.L., Seigh, J.W., Wilson, M.T., Gillies, I.P., Wright, J.J.: The sleep cycle modelled as a cortical phase transition. J. Biol. Phys. **31**, 547–569 (2005), doi:10.1007/s10867-005-1285-2
45. Steyn-Ross, D.A., Steyn-Ross, M.L., Wilson, M.T., Sleigh, J.W.: White-noise susceptibility and critical slowing in neurons near spiking threshold. Phys. Rev. E **74**, 051920 (2006), doi:10.1103/PhysRevE.74.051920
46. Steyn-Ross, M.L., Steyn-Ross, D.A., Sleigh, J.W., Liley, D.T.J.: Theoretical electroencephalogram stationary spectrum for a white-noise-driven cortex: Evidence for a general anesthetic-induced phase transition. Phys. Rev. E **60**(6), 7299–7311 (1999)

47. Strogatz, S.H.: Nonlinear Dynamics and Chaos: With Applications to Physics, Biology, Chemistry, and Engineering. Addison-Wesley, Reading, Mass. (1994)
48. Wilson, H.R., Cowan, J.D.: A mathematical theory of the functional dynamics of cortical and thalamic nervous tissue. Kybernetik **13**, 55–80 (1973)
49. Wilson, H.R.: Spikes, Decisions, and Actions: The Dynamical Foundations of Neurosciences. Oxford University Press, Oxford, New York (1999)
50. Wright, J.J., Liley, D.T.J.: Dynamics of the brain at global and microscopic scales: Neural networks and the EEG. Behav. Brain Sci. **19**, 285–309 (1996)